

RESEARCH ARTICLE

10.1002/2016JA022495

Special Section:

Measurement Techniques in Solar and Space Physics: Optical and Ground-Based

Key Points:

- Characteristics of acoustic gravity waves at Wallops Island
- Comparison with theoretical dispersion relation
- Propagation characteristics of traveling ionospheric disturbances

Correspondence to:

C. Negrea,
Catalin.Negrea@noaa.gov

Citation:

Negrea, C., N. Zobotin, T. Bullett, T. Fuller-Rowell, T.-W. Fang, and M. Codrescu (2016), Characteristics of acoustic gravity waves obtained from Dynasonde data, *J. Geophys. Res. Space Physics*, 121, 3665–3680, doi:10.1002/2016JA022495.

Received 4 FEB 2016

Accepted 23 MAR 2016

Accepted article online 30 MAR 2016

Published online 23 APR 2016

Characteristics of acoustic gravity waves obtained from Dynasonde data

Cătălin Negrea^{1,2,3,4}, Nikolay Zobotin^{1,2}, Terrence Bullett^{2,5}, Tim Fuller-Rowell^{2,3}, Tzu-Wei Fang^{2,3}, and Mihail Codrescu³¹Department of Electrical, Computer and Energy Engineering, University of Colorado Boulder, Boulder, Colorado, USA,²Cooperative Institute for Research in Environmental Sciences, University of Colorado Boulder, Boulder, Colorado, USA,³Space Weather Prediction Center, National Oceanic and Atmospheric Administration, Boulder, Colorado, USA, ⁴Institute of Space Science, Măgurele, Romania, ⁵National Centers for Environmental Information, National Oceanic and Atmospheric Administration, Boulder, Colorado, USA

Abstract Traveling ionospheric disturbances (TIDs) are ubiquitous in the thermosphere-ionosphere and are often assumed to be caused by acoustic gravity waves (AGWs). This study performs an analysis of the TID and AGW activity above Wallops Island, VA, during October 2013. The variations in electron density and ionospheric tilts obtained with the Dynasonde technique are used as primary indicators of wave activity. The temporal and spectral characteristics of the data are discussed in detail, using also results of the Whole Atmosphere Model (WAM) and the Global Ionosphere Plasmasphere Model (GIP). The full set of propagation parameters (frequency, and the vertical, zonal and meridional wave vector components) of the TIDs is determined over the 160–220 km height range. A test of the self-consistency of these results within the confines of the theoretical AGW dispersion relation is devised. This is applied to a sample data set of 24 October 2013. A remarkable agreement has been achieved for wave periods between 52 and 21 min, for which we can rigorously claim the TIDs are caused by underlying acoustic gravity waves. The Wallops Island Dynasonde can operate for extended periods at a 2 min cadence, allowing determination of the statistical distributions of propagation parameters. A dominant population of TIDs is identified in the frequency band below 1 mHz, and for it, the distributions of the horizontal wavelengths, vertical wavelengths, and horizontal phase speeds are obtained.

1. Introduction

Acoustic gravity waves (AGWs) are known to have an important impact on the dynamics of the upper atmosphere because of their role in transporting energy and momentum [Fritts and Alexander, 2003]. The perturbations due to wave propagation at ionospheric heights are typically observed using traveling ionospheric disturbances as tracers [Shiokawa et al., 2003; Kotake et al., 2006; Nicolls et al., 2004; Bristow et al., 1996; Ishida et al., 2008; Frissell et al., 2014; Vadas and Crowley, 2010; Oliver et al., 1994, 1995; Nicolls and Heinselmann, 2007; Djuth et al., 2010]. The dissipation of AGWs can have significant effects on the global dynamics of the thermosphere via momentum deposition [Yigit et al., 2009; Liu et al., 2013; Vadas et al., 2014]. Depending on the modulation of the thermospheric AGW spectrum, this process can impact the spectrum of tidal waves [Orland and Alexander, 2006; Vadas et al., 2014]. Finally, the AGW flux affects the long-term trends of the thermosphere-ionosphere system [Oliver et al., 2013].

A single harmonic of an acoustic gravity wave may be approximated locally (and within a very narrow altitude interval) by a plane wave model, which is characterized by a small set of parameters: frequency, horizontal and vertical wavelength, phase, propagation direction, and amplitude:

$$p = p_0(\omega) \exp[i(\mathbf{k} \cdot \mathbf{r} - \omega t)], \quad (1)$$

where p describes variations of a physical parameter of the medium (e.g., temperature and density), p_0 is the amplitude of these variations, \mathbf{k} is the wave vector, \mathbf{r} is the position vector, $\omega = \omega_0 + \mathbf{k} \cdot \mathbf{u}$ is the ground-based angular frequency, $\omega_0 = \frac{2\pi}{\Delta T}$ is the intrinsic frequency, ΔT is the wave period, t is the time, and \mathbf{u} is the background neutral wind velocity. All other relevant parameters (group velocity, phase speed, energy, and momentum) can be obtained from the prescribed set. Unfortunately, determining the full set is a challenging task, established techniques being able to provide some subset of parameters with either limited (i) altitude [Shiokawa et al., 2003; Frissell et al., 2014] or (ii) temporal coverage [Nicolls et al., 2012, 2014].

The scarcity of comprehensive data on thermospheric AGWs, coupled with the general lack of collocated measurements of the background horizontal winds, has made it difficult to accurately test the agreement between measurement derived wave parameters and the theoretical dispersion relation. The issue becomes a vitally important one in the case of ionospheric measurements, since AGWs are not the only possible cause for traveling ionospheric disturbances (TIDs). Interesting enough, this issue is rarely discussed in the existing literature. Comparisons between measurements and theoretical predictions have been performed for a single-wave mode detected at several altitudes, showing limited agreement [Nicolls and Heinselmann, 2007].

Obtaining the statistical distribution of the propagation characteristics of TIDs is of considerable interest. Several experimental techniques have been previously used for this goal [Ishida *et al.*, 2008; Grocott *et al.*, 2013; Shiokawa *et al.*, 2003; Hernandez-Pajares *et al.*, 2006; Nicolls and Heinselmann, 2007; Nicolls *et al.*, 2014]. However, the established methods currently do not allow the simultaneous determination of the full set of wave parameters over extended periods of time and over a significant height range.

We propose the use of Dynasonde data for the study of thermospheric gravity waves. For this first study, we used measurements obtained with the Vertical Incidence Pulsed Ionospheric Radar (VIPIR) instrument at Wallops Island, VA (37.85°N, 75.47°W), covering the whole month of October 2013. The Dynasonde analysis provides height profiles of electron density, zonal (west-east) and meridional (south-north) tilts, and vertical component of line-of-sight Doppler speed of plasma contours at all bottom ionosphere heights. The tilt measurements allow for horizontal components of the plasma density gradient to be obtained, from which the horizontal wavelength of TIDs can be extracted, while the vertical wavelength can be obtained directly from the height profile. Spectral analysis of the data is able to provide amplitudes of wave harmonics. In addition to this, the station can operate on a continuous basis, allowing very long time series to be obtained.

The purpose of this work is to (i) demonstrate the potential of Dynasonde-capable instruments to fully diagnose the AGW spectra and its altitude variability, (ii) study all spectral characteristics of the Dynasonde data, (iii) prove that the TIDs we observe accurately follow predictions of AGW theory, and (iv) determine the statistical distribution of AGW parameters for our sample data set from Wallops Island for October 2013. We believe this will bring an important contribution since the method allows for the full set of AGW parameters to be determined at all bottom *F* layer heights and Dynasonde-capable instruments can operate continuously.

The paper is structured as follows: section 2 describes the Dynasonde method and the data used, section 3 discusses the spectral features of our TID data, section 4 deals with the issues regarding the concurrent determination of the full set of AGW parameters and their agreement with the theoretical AGW dispersion relation, section 5 discusses the statistical distribution of the propagation characteristics of the AGW activity over Wallops Island, and section 6 summarizes our conclusions.

2. Dynasonde Data

The data set used in this study was obtained with the Wallops Island Dynasonde for the entire month of October 2013. The operation of Dynasonde-capable radars and analysis of their data are based on the Stationary Phase Group Range method [Paul *et al.*, 1974], requiring precise phase measurements by a number of receiver antennas. This is done for a sequence of pulses [Pitteway and Wright, 1992] optimized to provide high temporal and vertical resolution with very good associated uncertainties (typically smaller than 1%). For each echo a complete set of parameters is determined: group range, angle of arrival, doppler velocity, signal-to-noise ratio, and polarization. Based on these characteristics, echoes are grouped into traces. Those corresponding to secondary reflections and sporadic layers are excluded from the ionogram inversion. The inversion procedure, NeXTYZ [Zabotin *et al.*, 2006], determines the parameters of the so-called Wedge Stratified Ionosphere model, describing the local 3-D electron density distribution $N_e(\mathbf{r}, t)$. The model assumes a height-stratified ionosphere with each surface of constant electron density being a portion of a tilted plane. The horizontal components of the unit vector normal to this plane constitute the ionospheric tilts, n_x, n_y , used in this study:

$$\vec{n} = (n_x, n_y, n_z) = \frac{\nabla N_e}{|\nabla N_e|}. \quad (2)$$

More details of the Dynasonde operation and standard data analysis can be found in recent publications [Godin *et al.*, 2015; Negrea *et al.*, 2016] where this technique is applied in studies of ocean-thermosphere wave coupling and atmospheric tides.

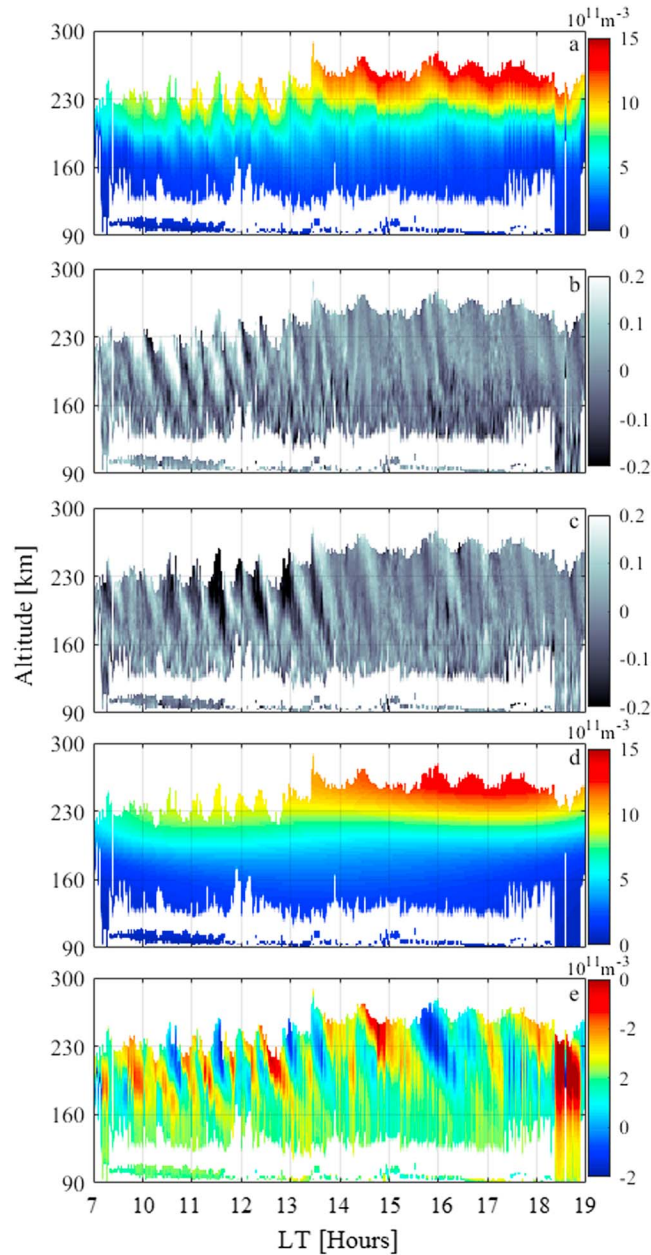


Figure 1. Data for Wallops Island, VA, on 24 October 2013: (a) electron density, (b) zonal (west-east) tilt, (c) meridional (south-north) tilt, (d) background electron density, and (e) electron density perturbation due to TIDs.

and T is the Earth’s rotation period. The horizontal components of the electron density gradient caused by TIDs (which utility for AGW studies was demonstrated by *Oliver et al.* [1994, 1995]) can be recovered from zonal and meridional tilts and the vertical component of the electron density gradient:

$$\nabla_x N_e = \frac{n_x \frac{\partial N_e}{\partial z}}{\sqrt{1 - n_x^2 - n_y^2}} - \frac{1}{c_E} \frac{\partial}{\partial t} \overline{N_e}, \tag{4}$$

$$\nabla_y N_e = \frac{n_y \frac{\partial N_e}{\partial z}}{\sqrt{1 - n_x^2 - n_y^2}}. \tag{5}$$

The raw electron density and tilt height profiles are obtained at a 2 min cadence, with a typical vertical resolution below 1 km. A linear interpolation procedure is used to obtain results on a 2 km resolution fixed height grid. In order to illustrate the dominant AGW activity, a 10 h sample data set obtained on 24 October 2013 is shown in Figure 1. All three quantities show perturbations indicative of AGW activity with tilted wave fronts and downward phase propagation. In Figure 1a, the background component of the electron density distribution, with its strong dependence on the altitude, is dominant. The same perturbations are more pronounced in the case of the two tilt measurements (Figures 1b and 1c).

Since utilization of the ionospheric tilts is currently unique to the Dynasonde method, it is necessary to discuss their properties and, in particular, why they act as a sensitive tracer for TIDs. For the purposes of data processing, one can assume that the spatiotemporal distribution of ionospheric plasma density, N_e may be represented in the vicinity of the station location as a sum of the background component $\overline{N_e}$, controlled primarily by exposure of the Earth’s atmosphere to the solar flux, and the disturbed component N'_e caused by the wave activity:

$$N_e(\mathbf{r}, t) = \overline{N_e}(\mathbf{r} - \hat{\mathbf{x}} c_E t) + N'_e(\mathbf{r}, t), \tag{3}$$

where $c_E = \frac{2\pi R_E \cos(L)}{T}$ is the Earth’s rotation speed at the station’s latitude L , R_E is the Earth’s radius,

The second term in equation (4) accounts for effects of the zonal gradients in the background electron density distribution. This correction term is significant mainly near the solar terminator. Time series of the plasma frequency profiles $N_e(z)$ and of the two tilt components, as shown in Figures 1a–1c, are products of autonomous Dynasonde data analysis. To distinguish between the background electron density distribution $\overline{N_e}$ and the electron density perturbations N'_e , an automated detrending procedure has been implemented, where $\overline{N_e}$ is approximated by a fourth-order polynomial at each constant altitude. The polynomial coefficients are determined through least squares fitting, and the resulting time series of the background electron density is presented in Figure 1d. The extracted disturbed component is displayed in Figure 1e. The slant wave front structures are similar to those in the tilt time series (Figure 1b and 1c). The partial derivatives $\frac{\partial}{\partial z} N_e$ and $\frac{\partial}{\partial t} \overline{N_e}$ present in equations (4) and (5) are obtained by a finite difference technique from the data series shown in Figures 1a and 1d.

Our processing technique is based on NeXtYZ output representing vertical profiles of various physical parameters describing the ionosphere. Altitude resolution of these profiles is high (2 km) and the data from every 2 km interval are processed independently. This justifies a use of a plane wave model for local representation of a single TID harmonic, similar to the one introduced by equation (1) for local representation of an AGW harmonic:

$$N'_e = N'_e(\omega) \exp[i(\mathbf{k} \cdot \mathbf{r} - \omega t)], \quad (6)$$

where $N'_e(\omega)$ is the magnitude of that specific harmonic, \mathbf{k} and ω are its wave vector and angular frequency, \mathbf{r} is the position vector, and t is the time. Function $N'_e(\omega)$ may have several local maxima corresponding to several wave packages with different carrier frequencies ω_j passing over the station at the same time. It follows from equation (6) that there is a linear relationship between the spectral amplitudes of the perturbation of the electron density gradient and the perturbation of the electron density itself:

$$\nabla N'_e = i\mathbf{k}N'_e. \quad (7)$$

We have shown earlier how the time series of the electron density perturbations and the time series of the horizontal gradients related to the wave activity can be obtained from the Dynasonde data. Equation (7) provides a tool for obtaining two horizontal components of the wave vector, k_x and k_y . An underlying assumption here is that there is only one wave vector \mathbf{k} corresponding to any specific frequency ω . The technique does not allow resolving wave packages propagating at the same carrier frequency and at the same time in different directions. This is a fundamental limitation for one-point measurements and it can be overcome only if observations are performed at several locations.

In a linear approximation with relation to the wave-related perturbations, real parts of the spectral amplitudes of the tilts can be expressed using equations (2) and (7) as

$$n_{x,y} = \frac{k_{x,y}}{|\nabla \overline{N_e}|} N'_e. \quad (8)$$

The normalization by the magnitude of the electron density gradient, $|\nabla \overline{N_e}|$, explains the reduced sensitivity of the tilts to altitude variations in the background electron density. This feature was noted with regard to the data presented in Figures 1a–1c.

3. Spectral Features

To determine the spectral features due to AGW activity in the data, an implementation of the Lomb-Scargle method is used [Lomb, 1976; Scargle, 1982, 1989; Press and Rybicki, 1989]. This is a preferred approach due to the presence of data gaps in the time series. Both magnitude and phase of the spectral components are of interest, and they are calculated using the approach suggested by Hocke and Kämpfer [2009]. A sliding window technique determines the time variation of the spectra, with a window length of 2 h and a step of 2 min.

It is usually the case that a superposition of several wave packages characterized by different carrier frequencies is observed. Because of this reason, spectra of variations of various ionospheric parameters have several spectral peaks of magnitudes N'_{ej} at frequencies ω_j , where index j enumerates the wave packages, at any particular time. Figure 2a shows typical examples of the spectra of electron density (N'_e), zonal ($\nabla_x N_e$) and meridional ($\nabla_y N_e$) gradient components, and zonal (n_x) and meridional (n_y) tilts with about 10 peaks clearly

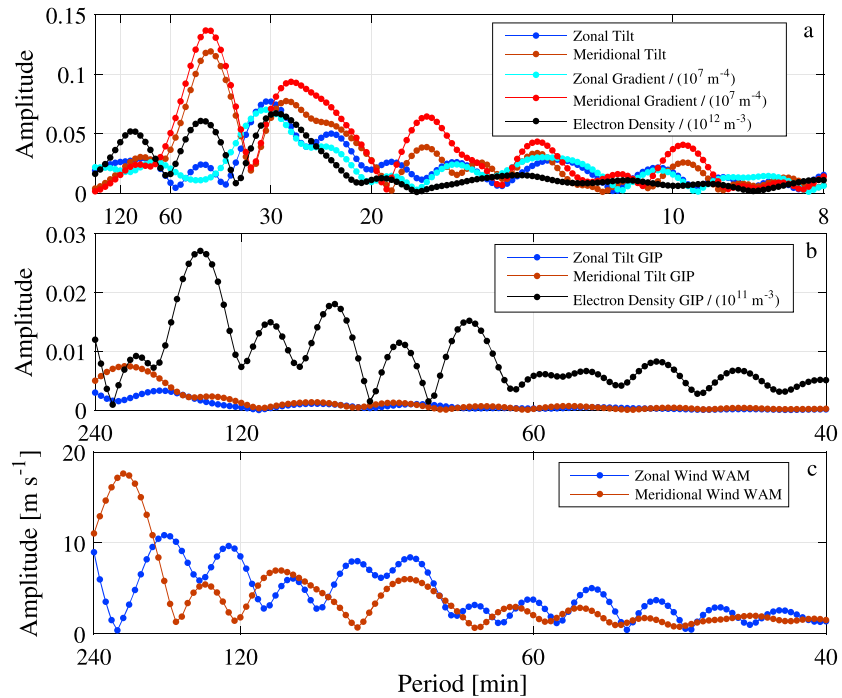


Figure 2. (a) Sample spectra at 200 km, for a time interval of 2 h centered at 10:16 LT on 24 October 2013. Frequency shifts can be observed between electron density and tilt spectral features and between zonal and meridional tilts. (b) Sample spectra of GIP electron density and synthetic tilts. (c) Sample spectra of the WAM neutral wind horizontal components.

identifiable. The spectra have been obtained with the same 2 h window, so they characterize the same wave field seen in different physical parameters. Nevertheless, there are both qualitative and quantitative differences between them. Such differences are quite expected because of two main reasons. First, gradients and tilts are vector quantities and sensitivity of their individual components to a wave package depends on its direction of propagation, while electron density variations are scalar. Second, “polarization relations” between pairs of physical quantities usually contain factors depending on the frequency (for example, in the equations (7) and (8) these are components of the wave vector \mathbf{k}), and therefore, equations determining positions of their extrema should have different roots. The latter is the most plausible explanation for subtle frequency shifts of the order of 10^{-5} Hz between the most prominent spectral peaks in the electron density and the two gradient components, as well as between $\nabla_x N_e$ and $\nabla_y N_e$, clearly visible in Figure 2a. While there are precedents for measuring plasma density gradients [Oliver *et al.*, 1994, 1995], to our knowledge this is the first report of the peculiarities of fine structures in their spectra.

When analyzing results of spectral measurements one should also bear in mind a possibility of distortions caused by (i) measurement errors or errors introduced by analysis techniques, (ii) effects introduced by the thermosphere-ionosphere coupling, and (iii) nonstationarity of the wave process within the 2 h window because of the tendency for the AGWs to propagate in packages. To explore influence of these factors, ionospheric model simulations were performed driven by representative and realistic neutral atmosphere waves. The Whole Atmosphere Model (WAM) [Akmaev *et al.*, 2008; Fuller-Rowell *et al.*, 2008] is a general circulation model for the neutral atmosphere. The model has 150 layers from the ground to a top pressure level close to 600 km and with layer thickness of a quarter scale height in the stratosphere and thermosphere. The model includes realistic dynamic forcing from the tropospheric and stratospheric waves so naturally generates a whole spectrum of resolved acoustic gravity waves, tides, and planetary waves. The horizontal resolution of 180 km and 3 min time step allows for a wave spectrum with horizontal wavelengths exceeding about 500 km and periods longer than about 20 min. Molecular dissipative processes, such as viscosity, heat conduction, and diffusion, tend to damp the waves in the upper thermosphere and naturally limit the vertical wavelength. Horizontal molecular transport of momentum, heat, and constituents along pressure surfaces are also included in the simulations. Additional physical processes incorporated in the extended model domain include UV and EUV radiative heating, infrared radiative cooling with the breakdown of local

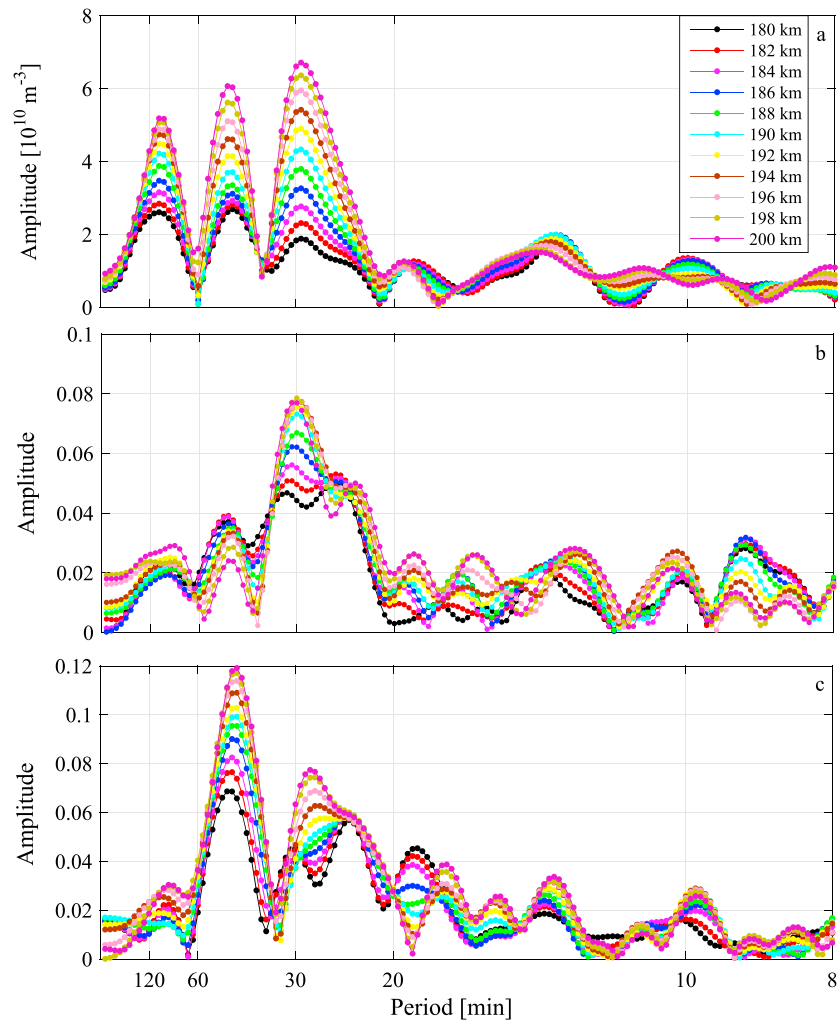


Figure 3. Height variation of the spectra obtained for Dynasonde data obtained at Wallops Island on 10:16 LT, 24 October 2013. (a) Detrended electron density, showing the TID amplitude, (b) zonal tilt, and (c) meridional tilt.

thermodynamic equilibrium, ion drag, and Joule heating. As well as analyzing the neutral atmosphere, the WAM global wave fields at 3 min temporal resolution were used to drive the Global Ionosphere Plasmasphere Model (GIP). GIP is a further development of the ionosphere-plasmasphere component of a coupled thermosphere-ionosphere plasmasphere model [Millward *et al.*, 1996]. It utilizes a Magnetic Apex coordinate system [Richmond, 1995] in which a global three-dimensional grid of magnetic field lines is created by tracing through the full International Geomagnetic Reference Field. The horizontal resolution is about $1^\circ \times 4.5^\circ$ in latitude-longitude. The dynamo electric field is calculated self-consistently by the electrodynamic solver of Richmond [1995] using the field line-integrated conductivities from GIP, and neutral winds, composition, and density from WAM. The electric fields, neutral winds, and composition were then used in GIP in the plasma density solution along the flux tubes, as well as the zonal and meridional plasma transport calculations. Both WAM and GIP were run under constant and quiet geomagnetic and moderate solar activity conditions ($F_{10.7} = 120$), so that any ionospheric variability (e.g., TIDs), including changes in the longitudinal structure from one day to the next, is entirely forced by the wave field propagating from below. Within the resolution limitation of WAM and GIP, the characteristic neutral waves and resultant TIDs should be reasonable consistent with the wave fields observed by the Dynasonde.

The GIP electron density at the grid points corresponding to the immediate vicinity of Wallops Island is used to calculate synthetic tilts in accordance with equation (2). Figure 2b shows spectra of electron density and zonal and meridional tilts derived from the GIP results. Similarly to Figure 2a, frequency shifts can be observed between

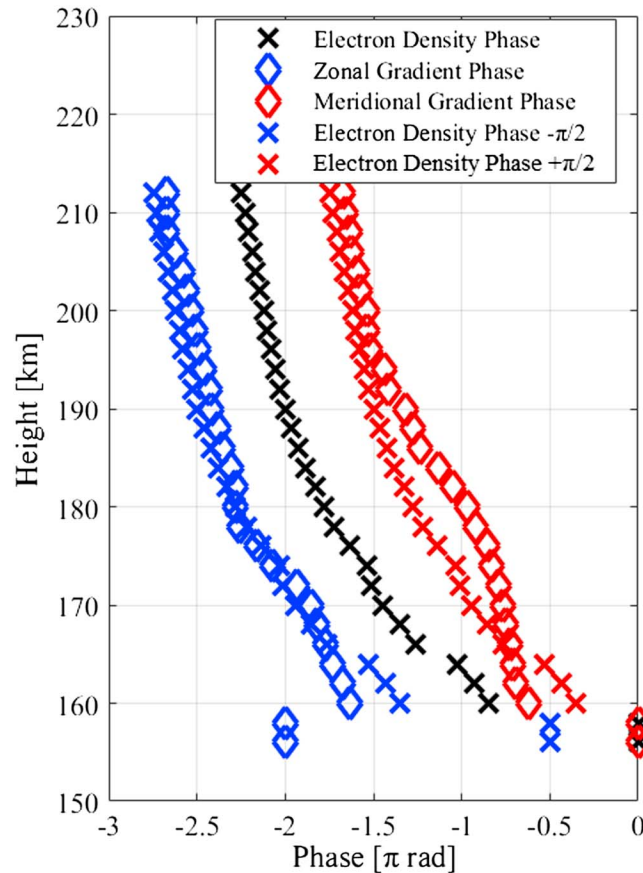


Figure 4. Height profile of the phase of the detrended electron density and the two horizontal components of the electron density gradient at a frequency of 0.55 mHz (30 min). The electron density phase is also shown with $+\frac{\pi}{2}$ and $-\frac{\pi}{2}$ offsets, highlighting the agreement between our data and the behavior of the phase theoretically predicted by equation (7).

Since ray paths are generally curved, the change in the propagation direction, coupled with changes in the neutral wind of 1–10 m/s, can account for Doppler-like frequency shifts.

Figure 3 shows an example of the altitude variation of the electron density (a) and tilt spectral magnitude (b and c) between 180 and 200 km. The TID amplitude (Figure 3a) shows a monotonic amplitude increase with height for periods higher than 18 min. The increase is not exponential and the amplitude difference between 180 and 200 km is smaller for higher frequencies, possibly due to increased attenuation and/or wave ducting. The tilt magnitudes have a much more complex variation with height, as they depend not just on the underlying AGW amplitude but also its wavelength and propagation direction. At frequencies where the TID amplitude is large, the difference in magnitude between the zonal and meridional tilt spectra is indicative of the wave’s propagation direction in the horizontal plane.

4. Wave Parameters

To fully characterize the TIDs observed at a certain location, in addition to the amplitude shown in Figure 3, all three components of the wave vector (zonal, meridional, and vertical) are required, at all frequencies, ideally over a wide altitude range. Equation (7) shows how the horizontal wave vector components can be determined from the spectra of the electron density and the electron density gradient. An estimate of the vertical wave vector component can be obtained experimentally from the height variation of the phase:

$$k_{zj} = \frac{\partial \Phi_j}{\partial z}, \tag{9}$$

spectra features in electron density and the tilts, as well as between the two tilt components. Simulation results strongly suggest that the frequency shifts among these parameters could be physically meaningful and are not an artifact due to data processing or measurement errors.

An analysis of the WAM neutral wind spectra (Figure 2c) diminishes point (ii) above as there are clear frequency shifts between the zonal and meridional wind components, similar to those observed between the zonal and meridional tilts. Since the GIP simulation used WAM wind fields as an input, it is a reasonable assumption that the frequency shifts observed in GIP results (Figure 2b) are linked to the frequency shifts in the WAM results (Figure 2c), and not by any anisotropies introduced by the geomagnetic field via the thermosphere-ionosphere coupling.

Nonstationarity of the wave process (propagation in packages) or of the atmosphere itself within the 2 h window cannot be excluded as factors influencing the spectrum shape. Since the spectra are functions of the ground frequency, the variation of the $\mathbf{k} \cdot \mathbf{u}$ product can be sufficiently large to produce observable effects.

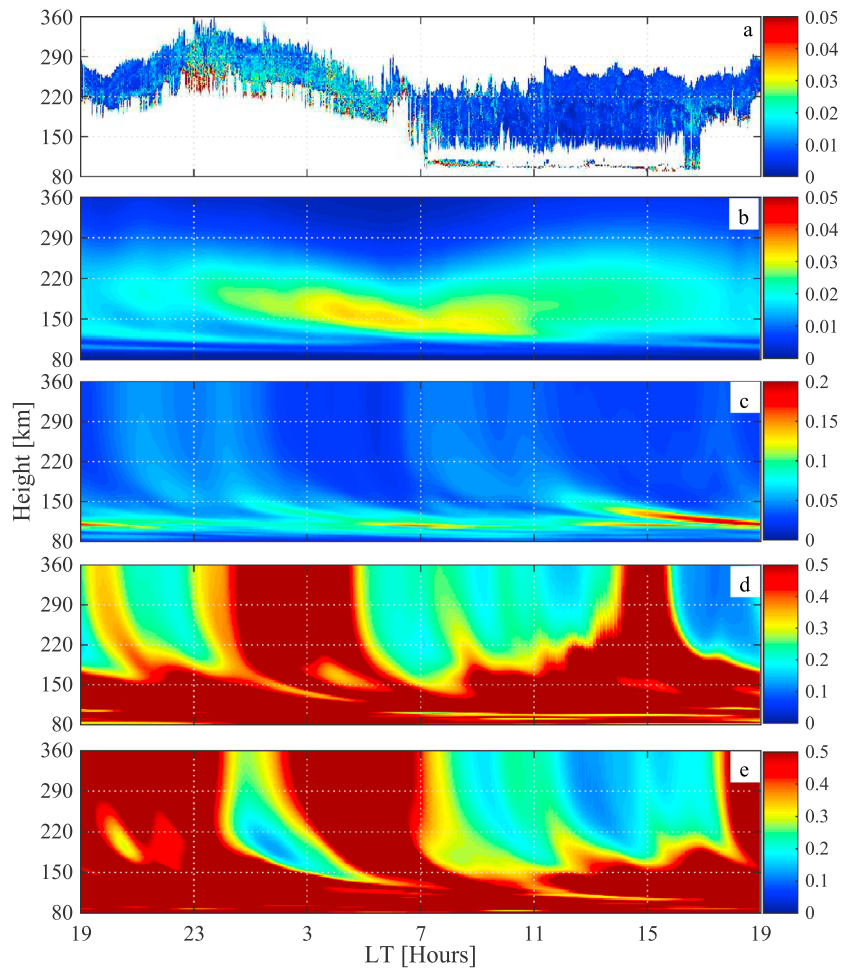


Figure 5. (a) Relative error of the Dynasonde electron density and the estimated uncertainty of the WAM, (b) mean molecular mass, (c) neutral temperature, and (d) zonal and (e) meridional neutral wind.

where Φ_j is the phase of the wave package j determined with a special implementation of the Lomb-Scargle algorithm [Hocke and Kämpfer, 2009] applied independently to data series from all available 2 km altitude intervals. The use of equation (9) means neglecting the vertical gradient of the Berry phase compared to k_z , what is usually a reasonable approximation [Godin, 2015]. It is also implied that the wave is in its propagation zone that it is not an evanescent one.

A natural question at this point is whether to use the phase of N'_e , $\nabla_x N_e$, or $\nabla_y N_e$. It is expected that values for k_z obtained using either electron density or the electron density gradient components should be similar. Equation (7) requires that there should only be a $\pm\frac{\pi}{2}$ phase difference between N'_e and both $\nabla_x N_e$ and $\nabla_y N_e$. Figure 4 shows the phase height profile for the wave package with central frequency 0.55 mHz (30 min period) for the three quantities and the time window centered at 10:16 LT. The phase of the electron density is also displayed with a $\pm\frac{\pi}{2}$ phase shift for comparison. The behavior is very close to what is expected theoretically. Figure 4 also shows that the choice of parameter to use in calculating k_z may not be obvious since the behavior of all three curves can be similar. However, N'_e will be preferred from now on, as it is obtained using a single data analysis product, the electron density, while the electron density gradient depends on both components of the tilt and the electron density.

Dynasonde analysis provides parameters of ionized component, which means that deriving parameters of neutral component requires additional steps and implies that results obtained without such extension

Table 1. Detailed Propagation Characteristics of the Three Dominant Wave Harmonics Highlighted in Figures 6 and 7: Frequency, Horizontal (λ_h) and Vertical (λ_z) Wavelength, Azimuth (Propagation Direction, θ), and Horizontal Phase Speed (v_h)

Frequency (mHz)	0.153	0.348	0.55
Period (min)	109	48	30
λ_h (km)	1025	335	368
λ_z (km)	155	112	209
θ (deg, direction)	102 (East)	185 (South)	134 (Southeast)
v_h (m/s)	277	93	199

describe TIDs that may not be always caused by acoustic gravity waves. For a wave with known frequency and wave vector components, it is theoretically possible to verify the agreement between measurements and the theoretical AGW dispersion relation

$$k_z = \sqrt{(k_x^2 + k_y^2) \left(\frac{N_0^2}{\omega_0^2} - 1 \right) + \frac{\omega_0^2}{C_0^2} + \frac{1}{4H^2}}, \quad (10)$$

where $N_0^2 = g \left(\frac{1}{H} - \frac{g}{C_0^2} \right)$, C_0 is the sound speed, H is the scale height, g is the gravitational acceleration, $\omega_0 = \omega - \mathbf{k} \cdot \mathbf{u} = \omega - k_x u_x - k_y u_y$, and u_x and u_y are the zonal and meridional components of the background neutral wind [Godin, 2015]. In practice, thermospheric AGWs can have a considerable imaginary component of k_z , both because there are large spatial regions where they may exist as evanescent waves and because of the viscous attenuation [Godin, 2014]. If a wave is in the shadow zone (this happens when the expression under radical sign in equation (10) is negative), it is still observable, but equation (9) is not valid: vertical gradient of the phase determines a different physical quantity. In our current analysis, we will assume that the observed wave packages are in propagation mode.

Theoretical estimate of k_z requires an accurate knowledge of the background atmospheric parameters. However, data on the neutral density, temperature, and winds are rarely available at thermospheric heights. One alternative is the use of results from numerical models, which can be accurate in a climatological sense. The uncertainty associated with model results can be difficult to estimate in the absence of comprehensive validation studies [Negrea et al., 2012], but errors between 10 and 20% are common [Fedrizzi et al., 2012]. In order to compare the propagation parameters we obtain with the theoretical dispersion relation, a month long WAM simulation was performed, for conditions corresponding to the month of October 2013, calculating neutral temperature, density, chemical composition, and both the zonal and meridional wind components. The background value for each parameter is assumed to be equal to the median of the whole 31 day interval, determined independently for each altitude and local time. The associated uncertainty is estimated by the corresponding standard deviation. Figure 5a shows the relative error for the Dynasonde-derived electron density for a 24 h long interval on 24 October 2013. The values are generally much smaller than 1%, while a minority of data points have relative errors of at most 5%. Figures 5b–5e show the estimated relative uncertainty for the mean molecular mass, neutral temperature, zonal wind, and meridional wind derived from WAM, all of which are higher than the uncertainty in the data. It is necessary to take into account the uncertainty associated with k_z and σ_{k_z} , due to the variability in the mean molecular mass, $\sigma_{\bar{M}}$, neutral temperature, σ_T , zonal wind, σ_{u_x} , and meridional wind σ_{u_y} (see Appendix).

For the three frequencies associated with dominant spectral peaks in Figure 3a (0.15, 0.33, and 0.55 mHz, or 109, 48, and 30 min, respectively), we determine k_x and k_y using equation (7) and k_z using equation (9). The characteristics of all three TIDs are listed in Table 1. Theoretical values for k_z are calculated using equation (10) with the uncertainties given by equations (A2.5)–(A2.9). A first comparison of the vertical wavelength ($\lambda_z = \left| \frac{2\pi}{k_z} \right|$) with respect to height is shown in Figure 6, covering the altitude interval 150–220 km. The agreement is good at 0.33 mHz (50 min) and reasonable at 0.55 mHz (30 min). Such a test of the agreement between data and the AGW dispersion relation helps to conclude that a TID is caused by an acoustic gravity wave. This test is successful for at least a part of the observed TID spectrum on 24 October 2013 over Wallops Island. Since the level of agreement seems to depend on frequency, a second comparison is performed with respect to frequency at 200 km altitude at 10:16 LT. Figure 7 shows qualitative agreement between the two sets of values for λ_z between 0.32 (52 min) and 0.8 mHz (21 min). Between 0.32 and 0.53 mHz there is a complete agreement within the calculated uncertainties. Between 0.53 (52 min period) and 0.8 mHz (21 min period) the experimental and theoretical values show the same trend, with some discrepancy in the case of extreme values. These may be due to the limitations in both equation (10) and in the model. For frequencies below

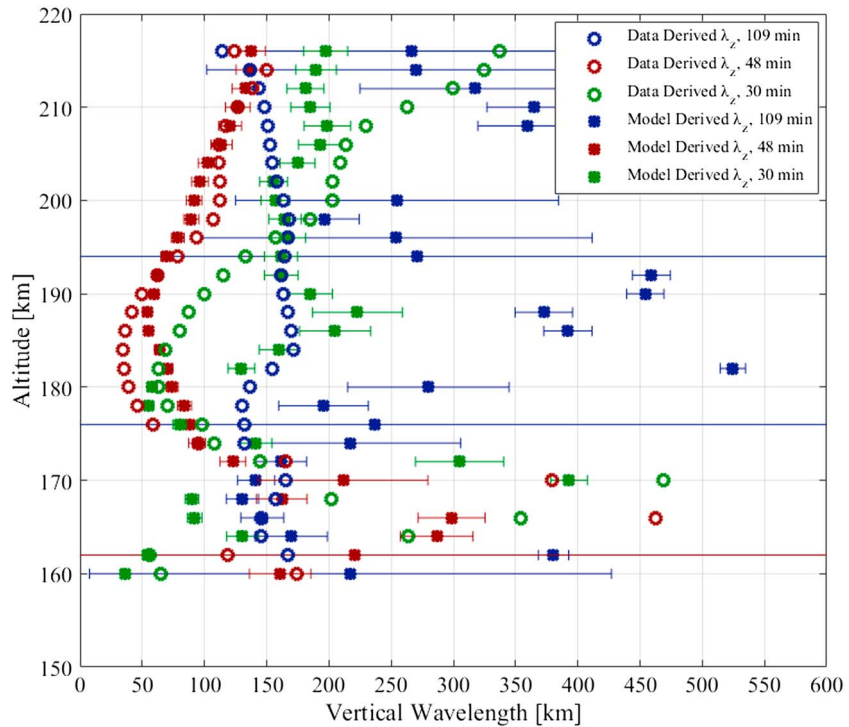


Figure 6. Comparison between the vertical wavelength obtained directly from the Dynasonde data with equation (9) and the model derived value obtained with equation (10), for the spectral peaks at 0.15, 0.33, and 0.55 mHz (109, 48, and 30 min, respectively) for the altitude range 150–220 km and the 2 h time interval centered around 10:16 LT 24 October 2013.

0.32 mHz and above 0.8 mHz, the test does not provide a definitive answer about the nature of the waves observed. This may be related to limitations of the equation (9) noted above. This is also reflected in the very large error bars associated with some of these values. Even partial, success of the test is remarkable. It suggests that the differences between the experimental and the theoretical values, where these are observed, are most likely due to deviations of the real atmospheric parameters from the median model values. Results of this kind may evolve into a potential measurement technique.

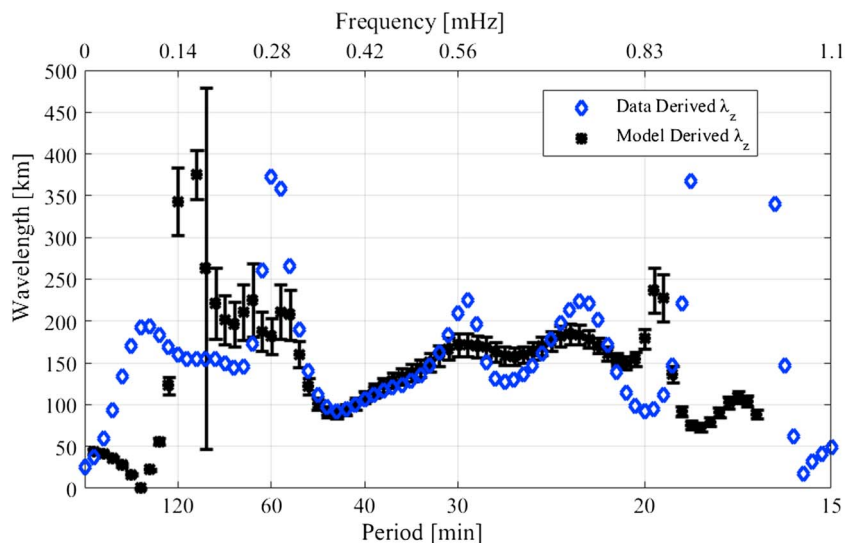


Figure 7. Same as Figure 6, but for the fixed altitude of 200 km and the frequency interval below 1 mHz.

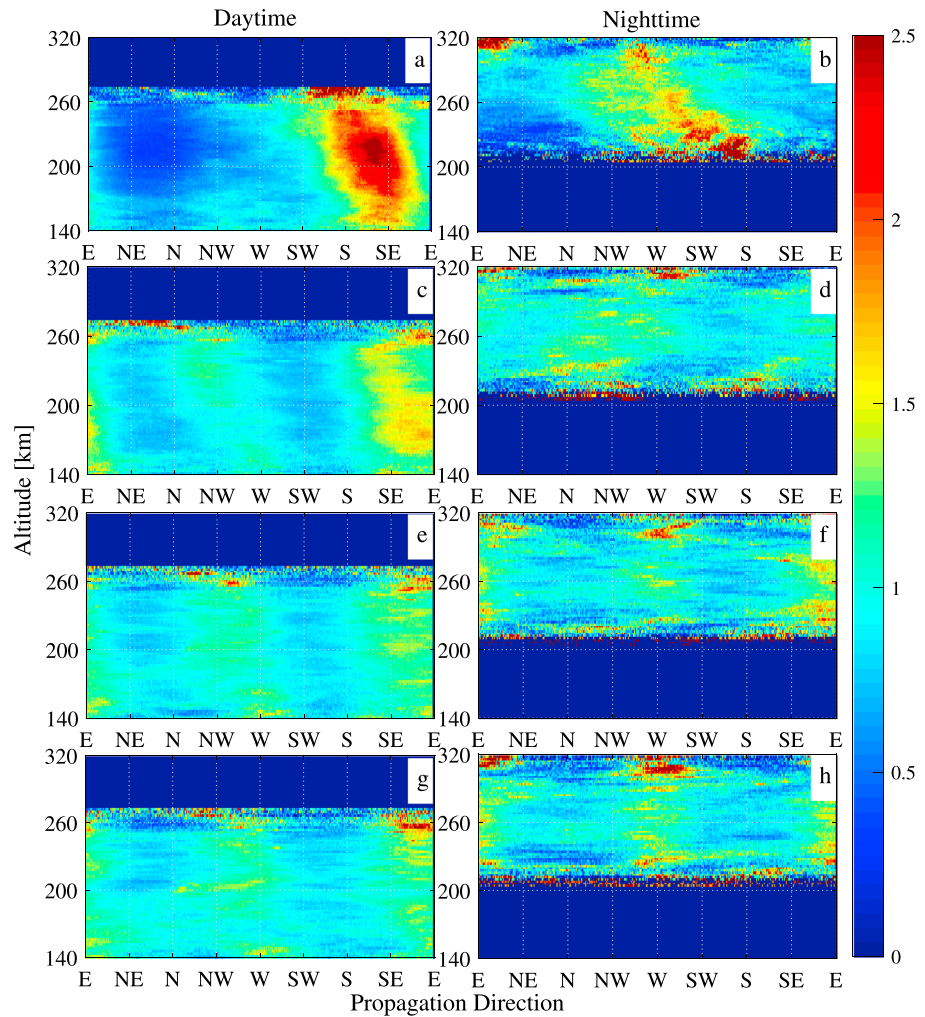


Figure 8. The statistical distribution of the horizontal propagation direction of observed TIDs as a function of altitude, separately for daytime and nighttime results, for the frequency bandwidth (a and b) below 1 mHz, (c and d) 1–2 mHz, (e and f) 2–3 mHz, and (g and h) 3–4 mHz. The results for each altitude and time interval are normalized by the number of data points corresponding to omnidirectional propagation.

5. Statistics of Propagation Parameters

The Dynasonde technique allows for the determination of all three wave vector components characterizing TIDs. This is accomplished using one of the normal operating modes of the station, without the need for a dedicated campaign. Due to this fact, large data sets can be obtained, allowing for the study of the variability in TID activity, on scales from several hours to months, or more. This is not a feature unique to Dynasonde instruments. However, the combination of both extensive temporal coverage and broad altitude range is currently unique. Electron density and tilt height profiles usually cover more than 100 km. The limitations of the technique are the inability to observe the “valley” between the ionospheric *E* and *F* layers, as well as the inability of ground-based HF radars to obtain data covering the topside ionosphere.

A sample data set covering the entire month of October 2013 is analyzed in this section. A sliding 2 h window is used at each altitude with a step of 2 min. The same Lomb-Scargle implementation as before is used to analyze spectral characteristics of the detrended electron density and the two horizontal components of the electron density gradient. k_{xy} is calculated using equation (7) and k_z is calculated using equation (9). First filter is applied by discarding any results for which there is a discrepancy of more than 4% between the integral of the Power Spectral Density and the time domain variance of either the zonal or the meridional tilts. This assures that results obtained at different altitudes will be comparable regardless of the specifics of

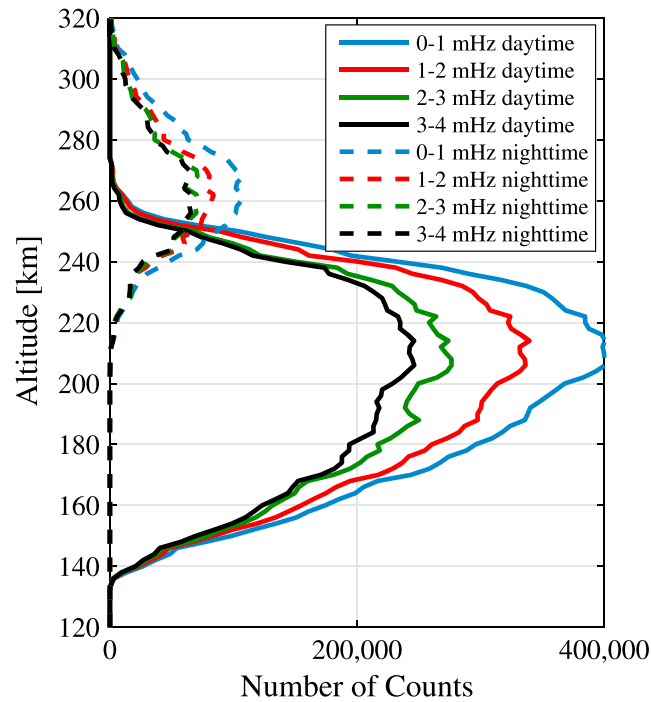


Figure 9. Total number of counts as a function of altitude and time of day for the four bandwidths (0–1 mHz, 1–2 mHz, 2–3 mHz, and 3–4 mHz) considered in Figure 8, with the solid line curves for daytime data and the dashed line curves for nighttime.

By contrast, results characterizing the nighttime ionosphere are obtained mostly for the altitude range 230–320 km. To avoid confusion between the diurnal variability and the altitude variation of the statistical distribution of TID parameters, we analyze the daytime and nighttime results separately, where for each day, “daytime” is defined as the time interval between local sunrise and sunset and “nighttime” as the time interval between local sunset and sunrise.

First, the azimuth associated with TID propagation is analyzed:

$$\theta = \text{atan} \frac{k_y}{k_x}. \tag{11}$$

In Figure 8, the distribution at each altitude is normalized by the number of data points expected within one bin in the case of omnidirectional propagation. The results show a strong dependence on frequency band (Figures 8a–8h). At frequencies below 1 mHz (periods larger than 17 min), a pronounced anisotropy is observed during daytime (Figure 8a), with the dominant wave population propagating south and southeast. Based on the results shown in Figures 6 and 7, it is reasonable to assume that acoustic gravity waves are the likely cause for these TIDs. There is a significant difference between the daytime (Figure 8a) and nighttime (Figure 8b) results. The predominant propagation direction switches toward the western direction, with an additional, associated decrease in the degree of anisotropy. It is difficult to determine from the data alone if (1) this transition is gradual and (2) if it is due to the change in local time or due to the change in altitude. At frequencies above 1 mHz (Figures 8c–8h), we observe a slight anisotropy, with two small TID populations propagating east and west, respectively, both during daytime (Figures 8c, 8e, and 8g) and nighttime (Figures 8d, 8f, and 8h). More analysis is necessary to establish if these are indeed caused by gravity waves or not. In addition to the fact that the observed anisotropy is small, the total number of data points decreases both with frequency and altitude (Figure 9).

In addition to the propagation direction, the horizontal ($\lambda_h = \frac{2\pi}{\sqrt{k_x^2 + k_y^2}}$) and vertical ($\lambda_z = \left| \frac{2\pi}{k_z} \right|$) wavelengths and the horizontal phase speed ($v_h = \frac{\omega}{\sqrt{k_x^2 + k_y^2}}$) are of interest. For the current study their distribution is determined

the data sampling [Negrea and Zobotin, 2016]. Second filtering algorithm first determines the median spectral amplitude for all local times, altitudes and frequencies and then discards all values less than that. An approach often used in the existing literature is to define a TID using a single prominent spectral peak characterized by a discrete, not necessarily fixed, frequency, active over a certain time interval. We believe this is problematic as TIDs usually produce multiple spectral features with varying bandwidths and duration. We are not interested in the statistical distribution of AGW or TID “events,” but rather the statistical characteristics of the TID activity as a whole. To accomplish this, all remaining valid data points are taken into account. Due to the natural ionospheric variability, results characterizing the daytime ionosphere are mostly obtained for the altitude range 140–260 km.

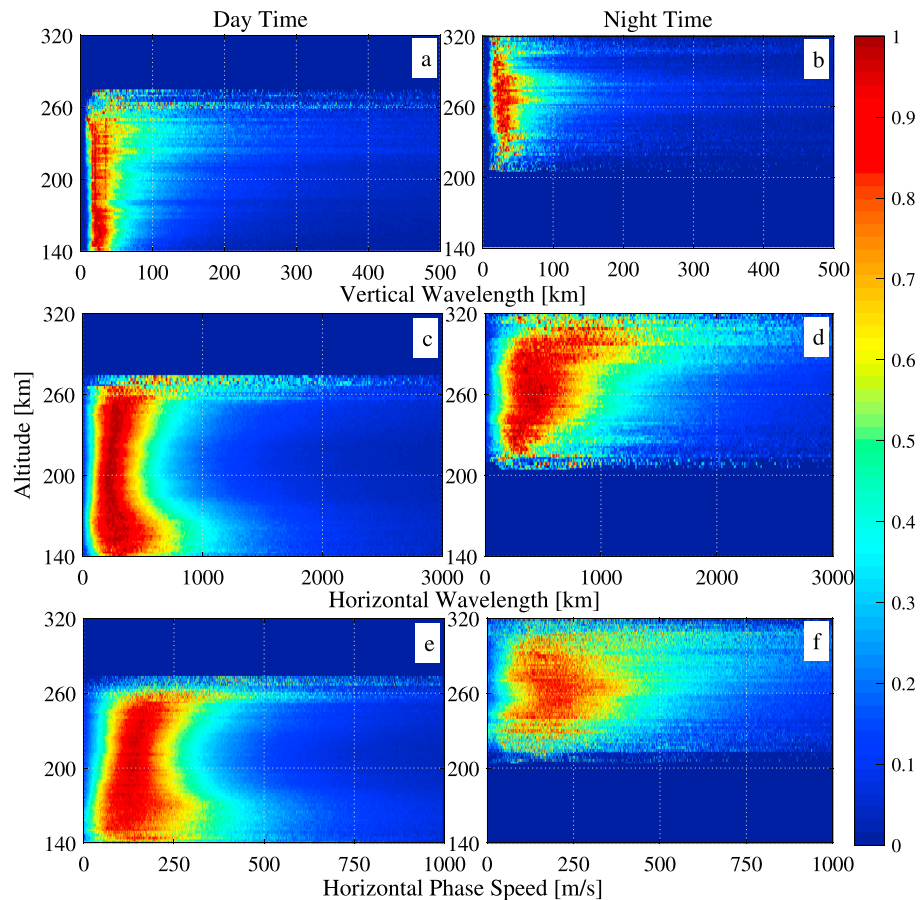


Figure 10. Statistical distribution of the TID (a and b) vertical wavelength, (c and d) horizontal wavelength, and (e and f) horizontal phase speed, separately for daytime and nighttime results. The results for each altitude and time interval are normalized by the maximum value for that altitude and time interval.

taking into account only TIDs with frequencies below 1 mHz, separately for daytime and nighttime measurements. For each altitude and parameter, the result is normalized by the maximum value for the respective time interval. The total number of counts depends strongly on altitude and local time, as seen in Figure 9. Most of the valid results in this case are between 150 and 250 km altitude during daytime, and between 240 and 270 km during nighttime, with the ratio of the daytime and nighttime maximum number of counts being approximately four to one. Figures 10c and 10e show daytime distributions dominated by a strong peak that widens and dissipates below 150 and above 250 km. The nighttime results (Figures 10d and 10f) show a considerably wider peak between 240 and 280 km. By contrast, the peak of the distribution of the vertical wavelength is wider in the altitude range 150–250 km during daytime (Figure 10a) and between 240 and 280 km during nighttime (Figure 10b), with most values about 30 km. The peak of the horizontal wavelength distribution is between 250 and 350 km during daytime and between 400 and 500 km during nighttime. Finally, the maximum of the phase speed distribution occurs between 100 and 180 m/s for daytime TIDs and between 180 and 220 m/s for nighttime TIDs.

It is interesting to note that the TIDs listed in Table 1 do not seem to be a part of the main TID population. This indicates that the AGWs with the highest amplitude for that specific time interval were not the source of the most numerous population of TIDs. The discussion in section 4 was focused on those spectral features clearly caused by gravity waves, which we verify by rigorously testing the agreement with the gravity wave dispersion relation (equation (10)). In Figures 8–10, we present the statistical distribution of TID propagation parameters, in accordance with the filtering and selection criteria detailed above.

6. Conclusions

In this paper, we analyze the characteristics of Dynasonde data measured above Wallops Island during the month of October 2013. Evidence of gravity wave induced TIDs is immediately obvious in the zonal and meridional ionospheric tilts. The same phenomenon is revealed in the electron density variations, with the help of an automated detrending procedure. Spectral analysis of the detrended electron density, horizontal components of the electron density gradients, and ionospheric tilts show the presence of small frequency shifts between the manifestations of the same wave mode in the different quantities. This is most likely due to changes in the wave propagation parameters within the 2 h window length we used.

The full set of propagation parameters is determined: the horizontal components of the wave vector using the electron density and the horizontal components of the electron density gradient and the vertical component of the wave vector using the variation of the wave phase with altitude. We test the agreement between our results and the theoretical gravity wave dispersion relation. In the altitude range 160–220 km, and for the frequency interval 0.32–0.8 mHz, the agreement is remarkable, taking into account the uncertainty associated with the parameters of the background thermosphere. Finally, the statistical distribution of the propagation parameters is analyzed. A dominant population of TIDs is identified, with frequencies below 1 mHz and a northwest to southeast propagation direction. For this frequency band, we analyze the altitude variation of the statistical distribution of the vertical wavelength, the horizontal wavelength and horizontal phase speed.

Finally, a few general remarks regarding the suitability of the products of the Dynasonde analysis software for the study of thermospheric acoustic gravity waves. The height profiles of the electron density and ionospheric tilts allow for the full set of AGW parameters to be determined for the bottomside ionosphere. By verifying the agreement of our results with the theoretical dispersion relation, we can identify the parts of the TID spectrum definitely caused by gravity waves. Finally, the continuous operation of Dynasonde-capable instruments allows comprehensive statistics to be obtained regarding the TID propagation parameters.

Appendix A

The model-derived vertical wave vector component obtained using equation (10) depends on the following parameters:

scale height

$$H = \frac{k_B T}{g \bar{M}}, \tag{A1}$$

sound speed

$$C_0^2 = \gamma k_B \frac{T}{\bar{M}}, \tag{A2}$$

buoyancy frequency

$$N_0^2 = g \left(\frac{1}{H} - \frac{g}{C_0^2} \right), \tag{A3}$$

and intrinsic wave frequency

$$\omega_0 = \omega - \mathbf{k} \cdot \mathbf{u} = \omega - k_x u_x - k_y u_y, \tag{A4}$$

where g is the gravitational acceleration, T is the neutral gas temperature, γ is the adiabatic index, k_B is the Boltzmann's constant, u_x and u_y are the zonal and meridional wind components, \bar{M} is the mean molecular mass, and ω is the ground-based frequency. We assume that the set of parameters $[\bar{M}, T, u_x, u_y]$ is

characterized by diagonal covariance matrix. The uncertainty associated with the model-derived vertical wave vector component is then

$$\sigma_{k_z}^2 = \left(\frac{\partial k_z}{\partial M}\right)^2 \sigma_M^2 + \left(\frac{\partial k_z}{\partial T}\right)^2 \sigma_T^2 + \left(\frac{\partial k_z}{\partial u_x}\right)^2 \sigma_{u_x}^2 + \left(\frac{\partial k_z}{\partial u_y}\right)^2 \sigma_{u_y}^2. \quad (\text{A5})$$

Using equation (10), it is straightforward to calculate the derivatives in equation (A5):

$$\frac{\partial k_z}{\partial M} = \frac{1}{2Mk_z} \left[\frac{1}{2H^2} + \frac{N_0^2}{\omega_0^2} (k_x^2 + k_y^2) + \frac{\omega_0^2}{C_0^2} \right], \quad (\text{A6})$$

$$\frac{\partial k_z}{\partial T} = \frac{-1}{2k_z} \left[\frac{1}{2H^2} - \frac{N_0^2}{\omega_0^2} (k_x^2 + k_y^2) - \frac{\omega_0^2}{C_0^2} \right], \quad (\text{A7})$$

$$\frac{\partial k_z}{\partial u_x} = \frac{-k_x}{2k_z} \frac{1}{C_0^2 \omega_0^3} \left[-g^2(\gamma - 1)(k_x^2 + k_y^2) + \omega_0^4 \right], \quad (\text{A8})$$

$$\frac{\partial k_z}{\partial u_y} = \frac{-k_y}{2k_z} \frac{1}{C_0^2 \omega_0^3} \left[-g^2(\gamma - 1)(k_x^2 + k_y^2) + \omega_0^4 \right]. \quad (\text{A9})$$

Acknowledgments

Authors thank O. A. Godin for stimulating discussions and helpful comments. This work was supported by the Office of Naval Research Basic Research Challenge program through award N000141310348. Field support of Wallops Dynasonde operation has been provided, in part, by the staff of the NASA's Wallops Flight Facility. The Dynasonde data are accessible through the project's web site (<http://surf.colorado.edu>) upon request to the author (N. Z. or T.B.) as well as through NGDC's MIRROR server (<ftp://ftp.ngdc.noaa.gov/ionosonde/data/WI937/>). This work utilized the University of Colorado Boulder research computing facility, which is supported by the National Science Foundation (award number CNS-0821794).

References

- Akmaev, R. A., T. J. Fuller-Rowell, F. Wu, J. M. Forbes, X. Zhang, A. F. Anghel, M. D. Iredell, S. Moorthi, and H.-M. Juang (2008), Tidal variability in the lower thermosphere: Comparison of Whole Atmosphere Model (WAM) simulations with observations from TIMED, *Geophys. Res. Lett.*, *35*, L03810, doi:10.1029/2007GL032584.
- Bristow, W. A., R. A. Greenwald, and J. P. Villain (1996), On the seasonal dependence of medium-scale atmospheric gravity waves in the upper atmosphere at high latitudes, *J. Geophys. Res.*, *101*(A7), 11,585–11,595, doi:10.1029/96JA01010.
- Djuth, F. T., L. D. Zhang, D. J. Livneh, I. Seker, S. M. Smith, M. P. Sulzer, J. D. Mathews, and R. L. Walterscheid (2010), Arecibo's thermospheric gravity waves and the case for an ocean source, *J. Geophys. Res.*, *115*, A08305, doi:10.1029/2009JA014799.
- Fedrizzi, M., T. J. Fuller-Rowell, and M. V. Codrescu (2012), Global Joule heating index derived from thermospheric density physics-based modeling and observations, *Space Weather*, *10*, S03001, doi:10.1029/2011SW000724.
- Frisell, N. A., J. B. H. Baker, J. M. Ruohoniemi, A. J. Gerrard, E. S. Miller, J. P. Marini, M. L. West, and W. A. Bristow (2014), Climatology of medium-scale traveling ionospheric disturbances observed by the midlatitude Blackstone SuperDARN radar, *J. Geophys. Res. Space Physics*, *119*, 7679–7697, doi:10.1002/2014JA019870.
- Fritts, D. C., and M. J. Alexander (2003), Gravity wave dynamics and effects in the middle atmosphere, *Rev. Geophys.*, *41*(1), 1003, doi:10.1029/2001RG000106.
- Fuller-Rowell, T. J., et al. (2008), Impact of terrestrial weather on the upper atmosphere, *Geophys. Res. Lett.*, *35*, L09808, doi:10.1029/2007GL032911.
- Godin, O. A. (2014), Dissipation of acoustic-gravity waves: An asymptotic approach, *J. Acoust. Soc. Am.*, *136*, EL411–EL417, doi:10.1121/1.4902426.
- Godin, O. A. (2015), Wentzel–Kramers–Brillouin approximation for atmospheric waves, *J. Fluid Mech.*, *777*, 260–290, doi:10.1017/jfm.2015.367.
- Godin, O. A., N. A. Zobotin, and T. W. Bullett (2015), Acoustic-gravity waves in the atmosphere generated by infragravity waves in the ocean, *Earth Planets Space*, *67*, 47, doi:10.1186/s40623-015-0212-4.
- Grocott, A., K. Hosokawa, T. Ishida, M. Lester, S. E. Milan, M. P. Freeman, N. Sato, and A. S. Yukimatu (2013), Characteristics of medium-scale traveling ionospheric disturbances observed near the Antarctic Peninsula by HF radar, *J. Geophys. Res. Space Physics*, *118*, 5830–5841, doi:10.1002/jgra.50515.
- Hernandez-Pajares, M., J. M. Juan, and J. Sanz (2006), Medium-scale traveling ionospheric disturbances affecting GPS measurements: Spatial and temporal analysis, *J. Geophys. Res.*, *111*, A07511, doi:10.1029/2005JA011474.
- Hocke, K., and N. Kämpfer (2009), Gap filling and noise reduction of unevenly sampled data by means of the Lomb-Scargle periodogram, *Atmos. Chem. Phys.*, *9*, 4197–4206, doi:10.5194/acp-9-4197-2009.
- Ishida, T., K. Hosokawa, T. Shibata, S. Suzuki, N. Nishitani, and T. Ogawa (2008), SuperDARN observations of daytime MSTIDs in the auroral and mid-latitudes: Possibility of long-distance propagation, *Geophys. Res. Lett.*, *35*, L13102, doi:10.1029/2008GL034623.
- Kotake, N., Y. Otsuka, T. Tsugawa, T. Ogawa, and A. Saito (2006), Climatological study of GPS total electron content variations caused by medium-scale traveling ionospheric disturbances, *J. Geophys. Res.*, *111*, A04306, doi:10.1029/2005JA011418.
- Liu, X., J. Xu, J. Yue, and S. L. Vadas (2013), Numerical modeling study of the momentum deposition of small amplitude gravity waves in the thermosphere, *Ann. Geophys.*, *31*, 1–14, doi:10.5194/angeo-31-1-2013.
- Lomb, N. R. (1976), Least-squares frequency analysis of unequally spaced data, *Astrophys. Space Sci.*, *39*, 447–462, doi:10.1007/BF00648343.
- Millward, G. H., R. J. Moffett, S. Quegan, and T. J. Fuller-Rowell (1996), A coupled thermosphere–ionosphere–plasmasphere model (CTIP), in *Handbook of Ionospheric Models*, edited by R. W. Schunk, STEP Rep., 239–279.
- Negrea, C., and N. A. Zobotin (2016), Mean spectral characteristics of acoustic gravity waves in the thermosphere-ionosphere determined from Dynasonde data, *Radio Sci.*, *51*, doi:10.1002/2015RS005823.
- Negrea, C., M. V. Codrescu, and T. J. Fuller-Rowell (2012), On the validation effort of the Coupled Thermosphere Ionosphere Plasmasphere Electrodynamics model, *Space Weather*, *10*, S08010, doi:10.1029/2012SW000818.
- Negrea, C., N. Zobotin, T. Bullett, M. Codrescu, and T. Fuller-Rowell (2016), Ionospheric response to tidal waves measured by dynasonde techniques, *J. Geophys. Res. Space Physics*, *121*, 602–611, doi:10.1002/2015JA021574.
- Nicolls, M. J., and C. J. Heinselmann (2007), Three-dimensional measurements of traveling ionospheric disturbances with the Poker Flat Incoherent Scatter Radar, *Geophys. Res. Lett.*, *34*, L21104, doi:10.1029/2007GL031506.
- Nicolls, M. J., M. C. Kelley, A. J. Coster, S. A. González, and J. J. Makela (2004), Imaging the structure of a large-scale TID using ISR and TEC data, *Geophys. Res. Lett.*, *31*, L09812, doi:10.1029/2004GL019797.

- Nicolls, M. J., S. L. Vadas, J. W. Meriwether, M. G. Conde, and D. Hampton (2012), The phases and amplitudes of gravity waves propagating and dissipating in the thermosphere: Application to measurements over Alaska, *J. Geophys. Res.*, *117*, A05323, doi:10.1029/2012JA017542.
- Nicolls, M. J., S. L. Vadas, N. Aponte, and M. P. Sulzer (2014), Horizontal parameters of daytime thermospheric gravity waves and E region neutral winds over Puerto Rico, *J. Geophys. Res. Space Physics*, *119*, 575–600, doi:10.1002/2013JA018988.
- Oliver, W. L., S. Fukao, Y. Yamamoto, T. Takami, M. D. Yamanaka, M. Yamamoto, T. Nakamura, and T. Tsuda (1994), Middle and upper atmosphere radar observations of ionospheric density gradients produced by gravity wave packets, *J. Geophys. Res.*, *99*(A4), 6321–6329, doi:10.1029/94JA00171.
- Oliver, W. L., S. Fukao, M. Sato, Y. Otsuka, T. Takami, and T. Tsuda (1995), Middle and upper atmosphere radar observations of the dispersion relation for ionospheric gravity waves, *J. Geophys. Res.*, *100*(A12), 23,763–23,768, doi:10.1029/95JA02520.
- Oliver, W. L., S.-R. Zhang, and L. P. Goncharenko (2013), Is thermospheric global cooling caused by gravity waves?, *J. Geophys. Res. Space Physics*, *118*, 3898–3908, doi:10.1002/jgra.50370.
- Ortland, D. A., and M. J. Alexander (2006), Gravity wave influence on the global structure of the diurnal tide in the mesosphere and lower thermosphere, *J. Geophys. Res.*, *111*, A10S10, doi:10.1029/2005JA011467.
- Paul, A. K., J. W. Wright, and L. S. Fedor (1974), The interpretation of ionospheric radio drift measurements-VI. Angle-of-arrival and group path [echolocation] measurements from digitized ionospheric soundings: The group-path vector, *J. Atmos. Terr. Phys.*, *36*, 193214, doi:10.1016/0021-9169(74)90040-3.
- Pitteway, M. L. V., and J. W. Wright (1992), Toward an optimum receiving array and pulse-set for the Dynasonde, *Radio Sci.*, *27*(4), 481–490, doi:10.1029/92RS00269.
- Press, W. H., and G. B. Rybicki (1989), Fast algorithm for spectral analysis of unevenly sampled data, *Astrophys. J.*, *338*, 277–280, doi:10.1086/167197.
- Richmond, A. D. (1995), Ionospheric electrodynamics using magnetic apex coordinates, *J. Geomagn. Geoelectr.*, *47*, 191–212.
- Scargle, J. D. (1982), Studies in astronomical time series analysis. II. Statistical aspects of spectral analysis of unevenly spaced data, *Astrophys. J.*, *263*, 835–853, doi:10.1086/160554.
- Scargle, J. D. (1989), Studies in astronomical time series analysis. III. Fourier transforms autocorrelation functions and cross-correlation functions of unevenly spaced data, *Astrophys. J.*, *343*, 874–887, doi:10.1086/167757.
- Shiokawa, K., C. Ihara, Y. Otsuka, and T. Ogawa (2003), Statistical study of nighttime medium-scale traveling ionospheric disturbances using midlatitude airglow images, *J. Geophys. Res.*, *108*(A1), 1052, doi:10.1029/2002JA009491.
- Vadas, S. L., and G. Crowley (2010), Sources of the traveling ionospheric disturbances observed by the ionospheric TIDBIT sounder near Wallops Island on 30 October 2007, *J. Geophys. Res.*, *115*, A07324, doi:10.1029/2009JA015053.
- Vadas, S. L., H.-L. Liu, and R. S. Lieberman (2014), Numerical modeling of the global changes to the thermosphere and ionosphere from the dissipation of gravity waves from deep convection, *J. Geophys. Res. Space Physics*, *119*, 7762–7793, doi:10.1002/2014JA020280.
- Yigit, E., A. S. Medvedev, A. D. Aylward, P. Hartogh, and M. J. Harris (2009), Modeling the effects of gravity wave momentum deposition on the general circulation above the turbopause, *J. Geophys. Res.*, *114*, D07101, doi:10.1029/2008JD011132.
- Zabotin, N. A., J. W. Wright, and G. A. Zhabankov (2006), NeXtYZ: Three-dimensional electron density inversion for Dynasonde ionograms, *Radio Sci.*, *41*, RS6S32, doi:10.1029/2005RS003352.